Saynisch, J., Irrgang, C., Thomas, M. (2018): On the Use of Satellite Altimetry to Detect Ocean Circulation's Magnetic Signals. - *Journal of Geophysical Research*, *123*, 3, pp. 2305—2314.

DOI: http://doi.org/10.1002/2017JC013742

Journal of Geophysical Research: Oceans

RESEARCH ARTICLE
10.1002/2017JC013742

On the Use of Satellite Altimetry to Detect Ocean Circulation's Magnetic Signals

J. Saynisch[1], C. Irrgang[1], and M. Thomas[1,2]

[1]Earth System Modelling, Helmholtz Centre Potsdam, GFZ German Research Centre, Potsdam, Germany, [2]Institute of Meteorology, Freie Universität Berlin, Berlin, Germany

Key Points:
- Sea surface height-based magnetic fields are derived using the geostrophic approximation
- The derived fields correlate well with the main features of the ocean circulation's magnetic signal
- A one-time calibration is advised to further improve the estimate's explained variance

Correspondence to:
J. Saynisch,
saynisch@gfz-potsdam.de

Citation:
Saynisch, J., Irrgang, C., & Thomas, M. (2018). On the use of satellite altimetry to detect ocean circulation's magnetic signals. *Journal of Geophysical Research: Oceans*, *123*, 2305–2314. https://doi.org/10.1002/2017JC013742.

Received 29 DEC 2017
Accepted 5 MAR 2018
Accepted article online 12 MAR 2018
Published online 30 MAR 2018

Abstract Oceanic magnetic signals are sensitive to ocean velocity, salinity, and heat content. The detection of respective signals with global satellite magnetometers would pose a very valuable source of information. While tidal magnetic fields are already detected, electromagnetic signals of the ocean circulation still remain unobserved from space. We propose to use satellite altimetry to construct proxy magnetic signals of the ocean circulation. These proxy time series could subsequently be fitted to satellite magnetometer data. The fitted data could be removed from the observations or the fitting constants could be analyzed for physical properties of the ocean, e.g., the heat budget. To test and evaluate this approach, synthetic true and proxy magnetic signals are derived from a global circulation model of the ocean. Both data sets are compared in dependence of location and time scale. We study and report when and where the proxy data describe the true signal sufficiently well. Correlations above 0.6 and explained variances of above 80% can be reported for large parts of the Antarctic ocean, thus explaining the major part of the global, subseasonal magnetic signal.

Plain Language Summary Oceans are a crucial part of Earth's climate system. Satellite magnetometers could pose as a unique and valuable source of oceanic information. Unfortunately, magnetic signals of ocean circulation are not jet detected from space. This manuscript proposes to use satellite altimetry as a by-pass to generate characteristic magnetic time series of the ocean circulation. These characteristic time series can subsequently be searched for with satellite magnetometers. If successful, this would allow to observe, for example, changes in the ocean heat budget.

1. Introduction

Despite the fact that oceans are a crucial part of Earth's climate system, their observability is far from satisfying. Existing global observation platforms, like satellite altimetry and gravimetry observe changes in a water column's mass and volume, properties that are sensitive to salinity, temperature, and mass anomalies. Satellite magnetometers like Swarm (Friis-Christensen et al., 2006) are able, at least in principle, to detect changes in a water column's conductance (Saynisch et al., 2017) which depends on salinity and temperature, too. In addition, satellite magnetometers are sensitive to the velocities in a water column (e.g., Tyler et al., 2003). Consequently, for oceanography, satellite magnetometers could pose a valuable addition to satellite altimetry and gravimetry.

Electromagnetic (EM) signals from ocean tides are already detected in satellite magnetometer observations (Tyler et al., 2003; Sabaka et al., 2015, 2016) suggest to use tidal signals to infer the conductivity of the lithosphere and upper mantle. Saynisch et al. (2016, 2017) propose to use EM tidal signals to estimate changes in the oceanic heat budget. Grayver et al. (2016, 2017) use EM tidal signals to derive information, like electrical conductivity and water content, about the upper 250 km of Earth's lithosphere and mantle. Still, the much desired signals of the ocean's general circulation remain undetected from space (Kuvshinov, 2008; Schnepf, 2017). However, local terrestrial measurements exist for a long time and studies demonstrate the respective principles (e.g., Larsen, 1991; Luther et al., 1991; Baringer & Larsen, 2001; Kuvshinov et al., 2006; Schnepf et al., 2014). The reason for the good detectability of tidal signals is their periodicity and consequently their high predictability. These predictions can be fitted to EM observations to estimate local tidal

amplitudes and phases (Tyler et al., 2003; Love & Rigler, 2014; Sabaka et al., 2015). By doing so, the information content of several consecutive observations is aggregated to improve the precision of amplitude and phase.

The ocean circulation emits magnetic signals with a standard deviation of 0.5 nT at sea surface (Irrgang et al., 2016a; Manoj et al., 2006). The strongest EM source is the Antarctic Circumpolar Current (ACC) whose transport correlates well with its total magnetic signal strength (Vivier et al., 2004). However, the separation of these signals from other EM sources is prevented by the ocean signal's erratic, or better, not well-known temporal behavior. The problem is even more challenging since the ACC is located in polar regions, where the signals from core, crust, and ACC are masked by signals from the ionosphere's polar electrojet. The separation of the nonerratic, i.e., static or trend, part of ocean circulation EM signals ($\pm$4 nT, Irrgang et al., 2016a) is prevented by other large constant or slowly varying contributions to the EM budget, e.g., from the core field and crustal magnetization (Kuvshinov, 2008).

In this study, we propose to use independent observations, i.e., satellite altimetry, to predict ocean circulation's EM signals. Satellite altimetry is considered one of the most reliable observational methods in physical oceanography (e.g., Egbert & Erofeeva, 2002; Chen et al., 2005; Le Bars et al., 2014). The geostrophic approximation (e.g., van Sebille et al., 2010; Ivchenko et al., 2011) is applied to sea surface height (SSH) to construct proxy EM predictions. However, to be able to evaluate the robustness of the proxy EM predictions, entirely model-based SSH are used in this study. The model derived EM proxies are then compared to the true EM signals of the same model simulation.

In analogy to tidal EM signals, altimetry-based EM predictions, if robust, would have a well-known temporal behavior which could be fitted to magnetometer observations to derive a local scaling amplitude. Consequently, this scaling amplitude and its anomalies could be exploited in analogy to tidal EM studies (Kuvshinov et al., 2006; Schnepf et al., 2014; Grayver et al., 2016, 2017), e.g., to estimate the oceanic heat budget (Saynisch et al., 2016). Such a product could also be used to remove the oceanic contributions from the observed EM budget.

To the same end, entirely ocean model generated EM signals could be fitted to magnetometer observations. However, modeled EM fields contain large uncertainties of up to 0.7 nT (Irrgang et al., 2016b). In addition, to use the benefits of EM data assimilation, EM observations that are independent of models are needed (Irrgang et al., 2017).

The geostrophic approximation and the design of the experiment are described in section 2. The used models for the ocean's general circulation and for the EM induction are described in section 3. Results are presented and discussed in section 4. We conclude and summarize in section 5.

2. Experiment Design

A 3-D global ocean circulation model (OMCT, see section 3) was forced with atmospheric reanalysis data to produce 11 years of realistic ocean circulation variability (Dobslaw et al., 2013). The simulation produces daily output for the years 2005 till 2015. From this data set, oceanic EM fields were derived in two different ways:

In the first approach (full information approach), we use the full information of the simulation. Oceanic electric conductivity (σ) is calculated from the ocean model's pressure (P), temperature (T), and salinity (S) distributions by using the Gibbs-SeaWater equation (TEOS-10, IOC, SCOR, and APSO, 2010). The 3-D conductivity distribution is combined with the ocean model's velocities ($\vec{u}$) to calculate oceanic electric sheet current density ($\vec{J}$):

$$\vec{J} = \int_{-H}^{0} \sigma(\vec{u} \times \vec{B}^{m})\, \mathrm{d}z, \tag{1}$$

where $\vec{B}^{m}$ is Earth's ambient magnetic field and H is the depth of the ocean floor. The electric currents are used as forcing in a 3-D induction solver (X3DG, see section 3) to calculate corresponding oceanic EM fields.

The second approach (geostrophic approach) uses only the model's SSH data and mimics the case when solely satellite altimetry observations are used. In this case the velocities are estimated from SSH using the geostrophic approximation (e.g., Woodworth et al., 1996; van Sebille et al., 2010; Ivchenko et al., 2011):

$$fu_{gy} = g\frac{d\eta}{dx},\ fu_{gx} = -g\frac{d\eta}{dy}, \tag{2}$$

where u_{gx} and u_{gy} are zonal and meridional geostrophic velocity, f is the local Coriolis parameter, η is the sea surface elevation, and g is Earth's gravitational acceleration. Note that if real satellite altimeter observations are used, spatial and temporal resolution as well as precision of the SSH gradients are nonhomogeneous and nonisotropic (e.g., Leeuwenburgh & Stammer, 2002). These properties depend on the respective satellite mission's inclination and repeat orbit. Along-track precision and resolution will usually be higher than cross-track precision. In this study of principle, these orbit effects are not considered.

To calculate geostrophic electric currents, $\vec{J_g}$, the geostrophic velocities are combined in equation (1) with climatological mean σ that was derived by using TEOS-10 with T and S values from the World Ocean Atlas (WOA, Conkright et al., 2002; Locarnini et al., 2013; Zweng et al., 2013). In future studies, this step can be omitted since a WOA-based oceanic conductivity data set is now available (Tyler et al., 2017). Note that temporal variations in σ can be neglected for annual and shorter time spans (Irrgang et al., 2016a). Oceanic electric currents calculated with WOA-based σ and OMCT-based σ locally differ by maximally 2%. As in the full information approach, the geostrophic approach's EM fields are calculated by using the $\vec{J_g}$ estimates as forcing for the X3DG induction solver (see section 3).

In section 4, the EM fields of both approaches are compared in different frequency bands. In this comparison, the EM fields of the full information approach are used as reference, i.e., as truth.

3. Models

Ocean velocities, SSH and seawater properties for the calculation of $\vec{J}$ and $\vec{J_g}$ are generated with the Ocean Model for Circulation and Tides (OMCT, Dobslaw & Thomas, 2007). The 1° baroclinic general circulation model uses nonlinear momentum equations. Despite the model's name, no tides are included in the simulations. The OMCT is forced with atmospheric reanalysis data from the European Center for Medium-Range Weather Forecasts (ECMWF, Uppala et al., 2008) and produces a realistic magnetic signal of the ocean's general circulation (Irrgang et al., 2016a, 2016b; Dobslaw et al., 2013). For the influence of the model resolution on the study, see Bingham and Hughes (2008). By applying the two approaches described in section 2 to the ocean model data, 11 years of daily electric currents for $\vec{J}$ and $\vec{J_g}$ are generated. The electric current fields have a resolution of 1°×1°.

The modeled electric currents from the two approaches are used to force the 3-D induction solver of (X3DG, Kuvshinov, 2008). X3DG calculates the EM fields in frequency space by a volume integral equation approach. In our configuration, a thin ocean and sediment layer of spatially variable electric conductance is assumed (Laske & Masters, 1997; Everett et al., 2003), in addition to a 1-D spherically symmetric mantle conductivity (Püthe et al., 2015). The forcing's frequency is set to zero. We calculate 1°×1° EM fields at sea level and at Swarm satellite altitude, i.e., 430 km above sea level.

With 1°×1° resolution, the calculation of EM fields uses considerable computational power. Therefore, for the whole time span, 2005–2015, only monthly mean EM fields from monthly mean $\vec{J}$ and $\vec{J_g}$ are calculated. In addition, daily EM fields are calculated for year 2005, the calibration year, and for 2015, the analysis year for short time variability (see section 4 for details).

4. Results and Discussion

The two approaches (section 2) are compared in terms of correlation and explained variance:

$$R_{EV} = 1 - \frac{var(B_z - B_{gz})}{var(B_z)}, \tag{3}$$

where B_z is the radial magnetic field from the full information approach, i.e., the supposed truth, and B_{gz} is the corresponding magnetic field from the geostrophic approach, i.e., is based on synthetic altimetry observations and WOA climatology. A R_{EV} of 1 corresponds to an explained variance of 100%, i.e., B_z and B_{gz} are identical.

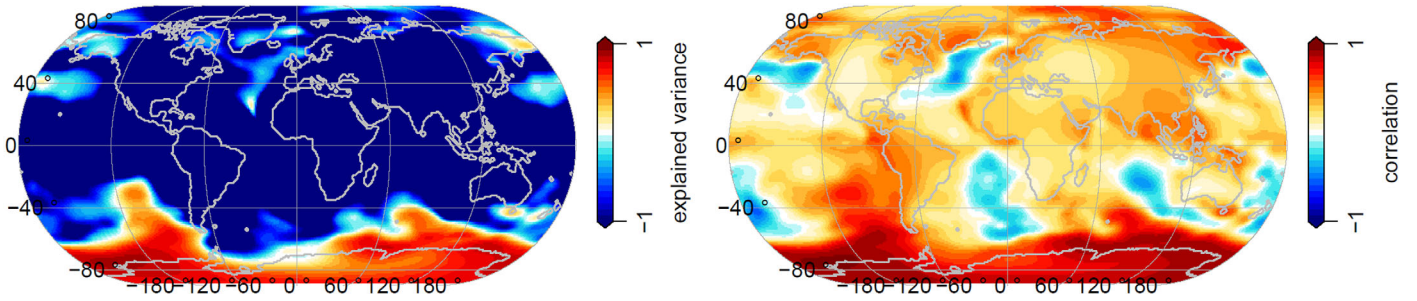

Figure 1. Analysis of subseasonal variability. Performance of the geostrophic approach with respect to the full information approach. Explained (left) variance and (right) correlation of year 2015 radial magnetic signals at satellite height.

Due to the aimed for application to satellite magnetometers (cf., section 1), the study focuses on B_z, which is the only oceanic magnetic signal measurable from space. However, note that at sea level the presented results are very similar for B_x, B_y, and B_z (not shown).

Due to large contrasts in ocean and land conductivity, electric fields are especially large in coastal regions. However, these are regions where the geostrophic approximation is less applicable. In addition, the proposed EM proxies based on satellite altimetry measurements will have lower precision near land (Vignudelli et al., 2005). Consequently, electric fields are not considered in this initial study.

The comparison will be done separately for subseasonal, seasonal, and decadal time scales. First, we focus on signals of subseasonal variability. Annual and longer variability is removed from the magnetic fields prior to the analysis. Figure 1 compares the daily fields of year 2015 of the geostrophic approach with respect to the full information approach. On the figure's left plot, the explained variance of the radial magnetic field at Swarm satellite height (430 km) is plotted.

In most parts of the globe R_{EV} is negative, i.e., the difference of B_{gz} and B_z has a larger variance than B_z alone. It becomes evident that the geostrophic approximation cannot be justified in all oceanic regions. The approximation is based on the assumption that the forces governing the ocean dynamics are the Coriolis force and the SSH-related pressure gradient. Processes, such as friction and acceleration, have to be negligible. These conditions are found in the open interior ocean, away from boundaries such as coasts and shelfs. By considering equation (2), it becomes evident that when f goes toward zero around the equator, the inversion becomes numerically unstable. By considering equation (1), one can see that the equator-problem is partly mitigated by the multiplication with $\vec{B}$. The vertical component of Earth's core field also reaches zero in equatorial regions. This component of $\vec{B}$ is most important for the oceanic fields which would be observable by spaceborne magnetometers. However, unrealistically high values of $\vec{u_g}$ and consequently $\vec{J_g}$ occur in this part of the ocean. In addition, no vertical velocity shear is included in the derivation of $\vec{u_g}$. Oceanic surficial, e.g., SSH-induced, pressure gradients become equilibrated with depth and the geostrophic currents are modulated accordingly. The depth of baroclinic compensation depends on the ocean's density stratification (e.g., Mellor, 1996), which increases from the poles to the equatorial region (Vinogradova et al., 2007). In summary, it is not astonishing that R_{EV} is negative in most regions.

In fact, the only region where the plain geostrophic approach gives useful information is the Southern Ocean. Here, up to 90% of the magnetic signal's subseasonal behavior is captured. Due to the colocation of the world's strongest current, the ACC, and the maximum of the magnetic core field, the Southern Ocean emits the strongest magnetic signals and the strongest variability (Vivier et al., 2004; Irrgang et al., 2016a). In this view, Figure 1 must be interpreted differently. The small area of the Southern Ocean where R_{EV} is at least 0.7 explains already 61% of the total global oceanic magnetic signal.

In contrast to the explained variance, the correlation of the magnetic fields (Figure 1, right plot) shows positive values in most areas of the globe. This means that the SSH contain information about the true EM signal's temporal behavior but the signal variances are different. This implies that temporal variations of $\vec{J}$ mainly go along with or are caused by variations in $\vec{u_g}$ resp. η. The reasons for the different variances are already discussed above. Interestingly, even around the equator the correlation of the two approaches is positive. Unexpected are the large areas of negative correlation in the interior of the large ocean basins.

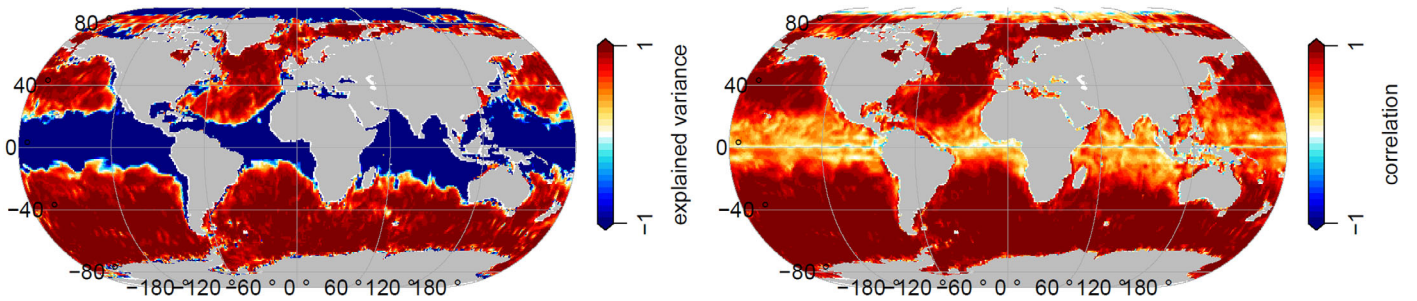

Figure 2. Analysis of subseasonal variability. Performance of the geostrophic approach with respect to the full information approach. Explained (left) variance and (right) correlation of year 2015 zonal electric currents (at sea level).

These anomalies loosely follow the mid oceanic ridges. As discussed, the geostrophic approximation is supposed to be valid in these regions. To separate the effect of geostrophic approximation and EM induction, the explained variances and the correlation of $\vec{J}$ resp. $\vec{J}_g$ are plotted in Figure 2.

As expected (Vinogradova et al., 2007; Bingham & Hughes, 2008), the geostrophic approximation explains a large fraction of the subseasonal electric current variability, e.g., R_{EV} above 0.8, in regions away from coast and the tropics (left plot). Remember that $\vec{J}$ is based on σ modeled by OMCT while $\vec{J}_g$ uses constant σ from the WOA climatology (section 2). Obviously, these conductivity differences have negligible effect on the subseasonal time scales (cf., also Irrgang et al., 2016a). Globally, the R_{EV} of $\vec{J}_g$ are better than the R_{EV} of $\vec{B}_g$. Likewise, the correlation is positive globally and shows no anticorrelation in the large ocean basins (right plot). Comparing Figures 1 and 2, gives a good impression of the impact of the EM induction process. The Maxwell equations are solved globally and the tropical unrealistic $\vec{J}_g$ are electromagnetically coupled to the higher latitudes. As a result, the R_{EV} and correlations deteriorate globally in the transition from $\vec{J}_g$ to $\vec{B}_g$.

To avoid the negative influence of the tropical region, we remove the temporal variation in $\vec{J}_g$ between $\pm 15°$ latitude. The induction process is modeled using this modulated electric currents. The results are plotted in Figure 3. Compared to Figure 1, the explained variances and the correlation improve. The strong positive R_{EV} of the Southern Ocean reach further north and positive R_{EV} occurs in the Northern Hemisphere. The correlations become stronger globally. The global mean correlation improves from 0.26 to 0.42. However, small negative correlations remain in the interior of the ocean basins.

By considering the rather complex pattern of the explained variances of the electric currents (Figure 2), one can see that temporal freezing of a single latitude band is a rather crude first order approach. As a next step, the electric current data itself is used to derive a detailed map of the temporal freezing pattern. To achieve this, the plotted R_{EV} map from (Figure 2) could be transformed into a mask of {0,1} that is multiplied with $\vec{J}_g$. However, regions should be included where the temporal behavior of $\vec{J}_g$ and $\vec{J}$ mainly differs by its amplitude. In these regions the temporal variability is not entirely set to zero but is weighted accordingly, i.e., scaled or calibrated (cf., van Sebille et al., 2010). To combine masking and calibration in one operation, $\vec{J}_g$ is fitted to $\vec{J}$ from the full information approach at every grid point. The electric current data used for the scaling must not include the analysis year. Consequently, $\vec{J}_g$ of 2005 without any temporal filtering was

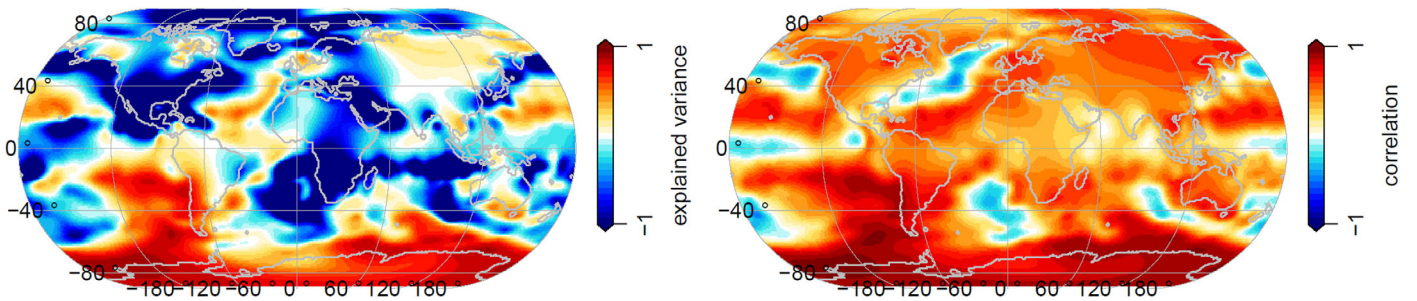

Figure 3. Analysis of subseasonal variability. Performance of the geostrophic approach where the tropical variability is removed. Explained (left) variance and (right) correlation of year 2015 radial magnetic signals at satellite height.

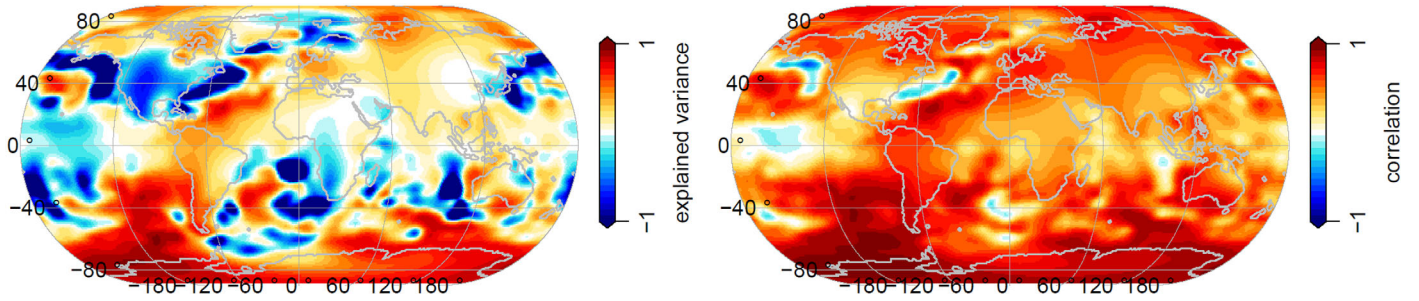

Figure 4. Analysis of subseasonal variability. Performance of the calibrated geostrophic approach with respect to the full information approach. Explained (left) variance and (right) correlation of year 2015 radial magnetic signals at satellite height. Calibration constants are derived from year 2005.

fitted to $\vec{J}$ of 2005. From the fit, only the local scaling constants are stored. Subsequently, the 2005 constants are applied to the $\vec{J}_g$ of year 2015, the analysis year. Consequently, year 2005 is omitted from all further analyses. The X3DG induction solver is forced with the calibrated $\vec{J}_g$ of year 2015 and the evaluated output is plotted in Figure 4.

In real-world applications, the scaling could be based entirely on modeled $\vec{J}$. However, alternatives exist, e.g., observation-based oceanic reanalyses (e.g., Forget et al., 2015), or observations of T, S, σ (e.g., Conkright et al., 2002; Locarnini et al., 2013; Zweng et al., 2013; Tyler et al., 2017), and $\vec{u}$ (e.g., Bonjean & Lagerloef, 2002; ESR, 2009) could be used to estimate characteristic variances of $\vec{J}$. Considering equation (1), we would like to point out that the calibration of $\vec{J}_g$ makes knowledge about σ, H, and $\vec{B}$ redundant since this information is already contained in $\vec{J}$. This means, $\vec{u}_g$ can be directly calibrated to have the same temporal variance as $\vec{J}$ (the units have to be adjusted). In other words, equations (1) and (2) can be combined in the following form:

$$\vec{J}_g \approx \vec{u}_g \times \vec{C} + \vec{D}, \tag{4}$$

where $\vec{C}$ and $\vec{D}$ are calibration constants (cf., van Sebille et al., 2010). This approximation implies that the temporal behavior of the oceanic electric currents is entirely determined by the behavior of SSH anomalies and their gradients. Note that in this form the vertical velocity shear is included. The baroclinic modulations of $\vec{u}_g$ can be interpreted as an effective integration depth $\hat{H}$. As long as the oceanic density stratification is not significantly changed, the baroclinic effect is included in the local integration constants.

Comparing Figures 1 and 4 shows a substantial gain in explained variance. The areas of high R_{EV}, e.g., above 0.8, grow and reach further North. Especially the southern Pacific shows now substantial positive R_{EV} corresponding to an explained variance of 80%. The same applies for the Gulf stream region. In general, most parts of the globe show positive R_{EV}, while the Antarctic remains unaffectedly good. Overall, the improvements are similar but stronger as in Figure 3. The coastal regions remain problematic. However, due to the shallow water, the radial magnetic signals are small in these regions (Irrgang et al., 2016a).

As expected, due to the calibration the explained variance resembles the correlation of the uncalibrated geostrophic approach (cf., left plot of Figure 4 with right plot of Figure 1). However, the correlation of the calibrated geostrophic approach with the true signal improved again. Globally, most of the correlations are now higher than 0.6. The global mean rises from 0.26 in the uncalibrated geostrophic approach to 0.49 in the calibrated geostrophic approach (cf., right plots of Figures 1 and 4). This further improvement is a bit unexpected since the calculation of correlations includes a scaling of variances, i.e., a calibration. In addition, correlations are still positive in areas where the explained variances are negative. The reason is again the nonlinearity of the induction process, i.e., the X3DG operator.

Given this insight, also the output of X3DG should be scaled. Consequently, we additionally calibrate $\vec{B}_g$ with respect to $\vec{B}$. In analogy to equation (4), the scaling constants are derived by least-square fitting of 2005's $\vec{B}_g$ to 2005's $\vec{B}$ without any prior temporal filtering. The derived scaling constants are then applied to year 2015's $\vec{B}_g$. This double-calibrated geostrophic approach is evaluated against the full information approach in Figure 5.

As a result of the double-calibration, the explained variances become positive globally. Since all processing after the X3DG is linear, the respective correlation changes no further. This justifies not only the applicability of the geostrophic approximation but also the assumption of equation (4) in regions of high R_{EV}. Especially

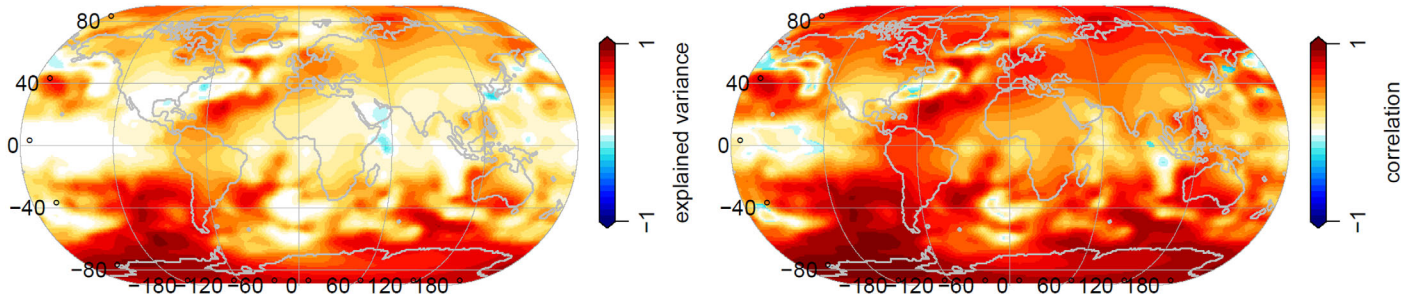

Figure 5. Analysis of subseasonal variability. Performance of the double-calibrated geostrophic approach with respect to the full information approach. Explained (left) variance and (right) correlation of year 2015 radial magnetic signals at satellite height. Calibration constants are derived from year 2005.

in the Southern Ocean where the EM signals are usually high, temporal variations of H, η, σ, and $\vec{B}$ lead only to negligible contributions to $\vec{J}$ resp. $\vec{B}$. Consequently, the choice of the scaling year barely influences the subseasonal results. The plotted correlation can be interpreted as a measure for the quality to expect from a fit of altimetry-based $\vec{B_g}$ to real satellite magnetometer observations (cf., section 1). Consequently, the correlation fields should be used as weights in such a fitting process.

To test if the scaling of the magnetic fields alone is sufficient, the calibration of $\vec{J_g}$ was omitted and only $\vec{B_g}$ was calibrated to 2005's $\vec{B}$. The respective R_{EV} are similar but smaller than the R_{EV} of the double-calibrated approach (not shown). However, calibrating only $\vec{B_g}$ gives better R_{EV} than calibrating only $\vec{J_g}$. Nonetheless, if the $\vec{B_g}$ should be fitted to EM observations, calibration of $\vec{J_g}$ is advised (cf., right plots of Figures 4 and 5). Remember that at each grid point, the $\vec{B_g}$ from the calibrated and the double-calibrated approach differ only by a scaling constant. Consequently, both time series are equally suitable to be fitted to EM observations, since their temporal behavior is the same and the fitting will replace any scaling of $\vec{B_g}$.

If the $\vec{B_g}$ should be used without a prior fit to EM observations then the calibration of $\vec{J_g}$ and $\vec{B_g}$ is recommended.

The previous analyses are repeated for the seasonal frequency band. Monthly mean fields of the years 2006–2015 from the OMCT ocean simulation are used to calculate $\vec{B}$ resp. $\vec{B_g}$. The monthly mean removes

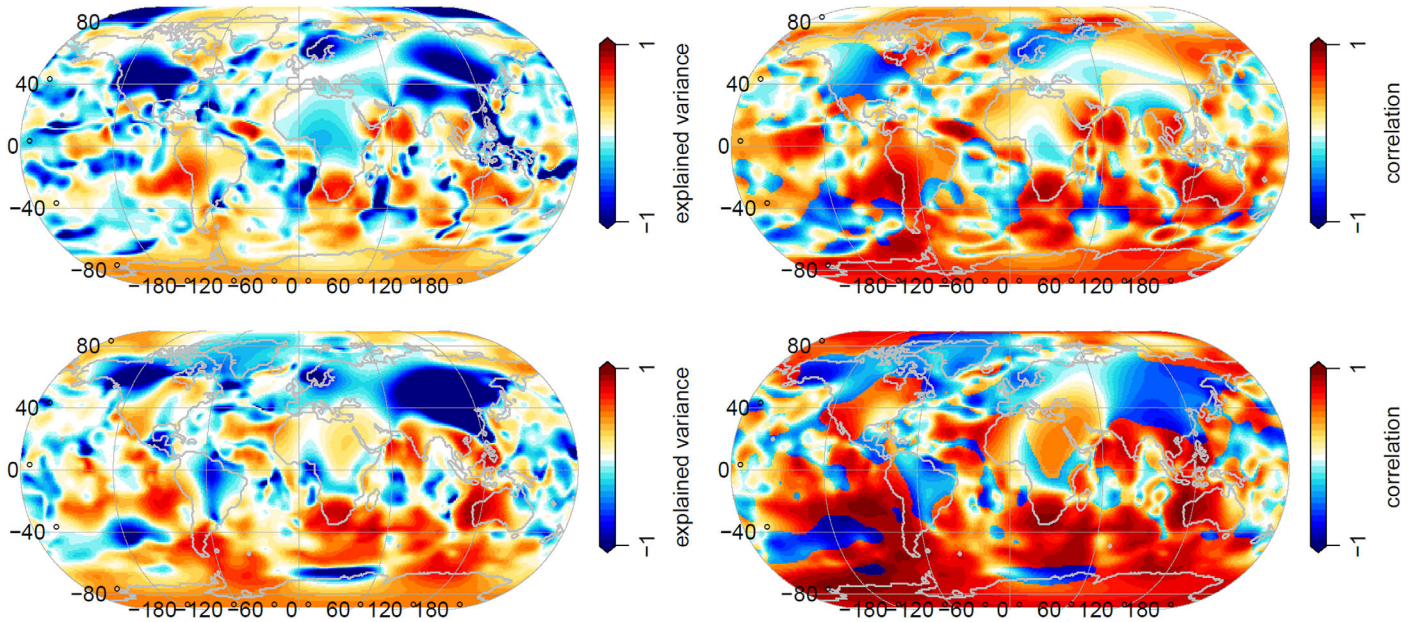

Figure 6. Analysis of seasonal variability. Performance of the double-calibrated geostrophic approach with respect to the full information approach. Explained (left) variance and (right) correlation of year 2015 radial magnetic signals at satellite height. Calibration constants are derived from year 2005. Bottom plot: steric contributions to SSH are removed before the geostrophic approach is applied.

the subseasonal variance. Decadal variations are removed in addition. Figure 6 (top plot) shows the evaluation of the double-calibrated geostrophic approach. As in the subseasonal analysis, the calibration of $\vec{J}_g$ and $\vec{B}_g$ are based on the year 2005.

The explained variances and correlations are significantly smaller than for the subseasonal time scales. Positive values now only cover small areas. Baroclinic processes are much stronger on seasonal time scales (Vinogradova et al., 2007). Consequently, the geostrophic approximation is less applicable. Furthermore, the assumption of constant $\vec{C}$ and $\vec{D}$ in equation (4) becomes less valid. Annual changes in the oceanic density field influence the effective integration depth $\hat{H}$. As a consequence, the results depend on the choice of the scaling year. Steric contributions to SSH have to be removed since they should not be interpreted as geostrophic velocities (Ivchenko et al., 2011; Willis et al., 2004). The respective explained variances and correlations slightly improve (Figure 6, bottom plot).

The analysis of the decadal time scales reveals further deterioration of explained variance and correlation (not shown). On these time scales, the oceanic variability is strongly baroclinic (cf., Vinogradova et al., 2007; Bingham & Hughes, 2008). In contrast to seasonal time scales (Irrgang et al., 2016a), on decadal time scales variations in σ contribute additionally to the variability of the EM signals (Saynisch et al., 2016). As with the seasonal time scale, steric SSH anomalies should be removed before $\vec{u}_g$ is derived. In real world applications, the secular variation of Earth's magnetic field would further add to the deterioration of explained decadal variances.

However, on seasonal and decadal time scales $\vec{B}_g$ can still be fitted to the magnetometer observations to identify changes in $\vec{C}$ and $\vec{D}$, i.e., changes in σ, $\hat{H}$, and oceanic heat content.

5. Summary and Conclusions

A global ocean model is utilized to test the use of satellite altimetry to reconstruct or detect nontidal oceanic magnetic signals. Daily modeled sea surface height (SSH) anomaly fields are converted into oceanic transport estimates via the geostrophic approximation. Based on these geostrophic transports, electric currents are estimated and used as forcing for an electromagnetic (EM) induction solver. The resultant SSH-based magnetic field proxies are evaluated against modeled magnetic fields that are based on the full information of the same ocean model simulation, i.e., salinity, temperature, and velocities. The results of the evaluation depend on location and considered time scale.

Good agreement between SSH-based magnetic fields and the magnetic fields that are based on the full model information are found in the Antarctic region for subseasonal time scales. The Antarctic Circumpolar Current emits the strongest and most variable oceanic magnetic signals (Irrgang et al., 2016a). Here, correlations of 1.0 and explained variances of 90% are found in large areas. For the remaining regions, calibration of the geostrophic estimates is advised (cf., van Sebille et al., 2010). The proposed scaling strategies result in positive correlations and explained variances globally.

On these short time scales, geostrophy and magnetic fields are strong in the same geographic regions. The geostrophic approximation fails in regions where the magnetic signals are small. Near coasts and in shallow water, where friction prevents a geostrophic balance, the water column's conductance is small. At the equator, the Coriolis parameter reaches zero and prevents a geostrophic balance. In the same area, the dip equator of the radial magnetic core field results in very small electric currents.

We conclude that SSH from satellite altimetry can be converted into proxy magnetic fields that, apart from a local scaling factor, would show the true temporal behavior of the subseasonal oceanic magnetic field in the identified regions. In analogy to tidal EM signals (Tyler et al., 2003), altimetry-based EM predictions could then be fitted directly to Swarm magnetometer observations to estimate the local scaling factor. Consequently, this scaling factor and its anomalies could be exploited in analogy to recent tidal EM studies (Kuvshinov et al., 2006; Schnepf et al., 2015; Grayver et al., 2016, 2017), e.g., to estimate the oceanic heat budget (Saynisch et al., 2016). Reapplication of these approaches may give valuable information in areas where the tidal EM signal is small while the ocean circulation's EM signal is strong, e.g., in the Bellingshausen Sea and the southern Indian Ocean. Furthermore, the fitted values contain information about oceanic conductivity and could be used for oceanic data assimilation (Irrgang et al., 2017) and to infer oceanic heat content (Saynisch et al., 2017). With or without a prior fit to observations, altimetry-based EM predictions could be

subtracted from Earth's observed magnetic field anomalies and may improve the observability of other EM sources, e.g., the ionosphere or crustal anomalies.

During the fitting or the subtraction, the correlations derived in this model study should be incorporated in the error budget of the respective mathematical operation.

For longer time scales, i.e., seasonal and decadal, the geostrophic approach in its proposed form loses its justification. The reasons are steric effects in SSH and baroclinic variability. On these time scales, SSH-based EM predictions might be improved by removing steric effects and including additional global observation systems. Operational products exist that statistically combine satellite observations of SSH and sea surface temperature with ARGO in situ measurements to generate 3-D data sets of salinity, temperature, and velocity (e.g., ARMOR3D L4 (weekly data), Mulet et al., 2012; Guinehut et al., 2012). However, this will introduce additional, unknown sources of errors. Evaluation of the robustness of respective EM estimates would require to reimplement the statistical methods in a model-only scenario. However, incorporation of oceanographic in situ observations would surely improve the seasonal and decadal time scales of SSH-based EM estimates. Still, the proxy magnetic fields could be fitted to magnetometer observations. The fitting constants and their anomalies could be used to infer information about steric and baroclinic processes as well as heat induced changes in oceanic conductivity.

Acknowledgments
This study has been funded by the Helmholtz Foundation and the German Research Foundation (SPP1788 Dynamic Earth). The authors thank for the opportunity to use ERA-Interim data from the European Centre for Medium-Range Weather Forecasts, the World Ocean Atlas, and facilities from the German High Performance Computing Centre for Climate, and Earth System Research. Atmospheric forcing data are available from www.ecmwf.int. The WOA data can be downloaded from https://www.nodc.noaa.gov/OC5/woa13/. We thank Alexey Kuvshinov (kuvshinov@erdw.ethz.ch) for the opportunity to use the 3-D EM induction solver X3DG. We thank two reviewers for their assistance on this manuscript. The derived explained variance of the electric currents can be downloaded from ftp.gfz-potsdam.de/pub/home/ig/saynisch/oc_induction/Rev/Jel.

References

Baringer, M. O., & Larsen, J. C. (2001). Sixteen years of Florida current transport at 27 degrees N. *Geophysical Research Letters*, *28*(16), 3179–3182. https://doi.org/10.1029/2001GL013246

Bingham, R. J., & Hughes, C. W. (2008). The relationship between sea-level and bottom pressure variability in an eddy permitting ocean model. *Geophysical Research Letters*, *35*, L03602. https://doi.org/10.1029/2007GL032662

Bonjean, F., & Lagerloef, G. S. E. (2002). Diagnostic model and analysis of the surface currents in the tropical Pacific Ocean. *Journal of Physical Oceanography*, *32*, 2938–2954.

Chen, J. L., Wilson, C. R., Tapley, B. D., Famiglietti, J. S., & Rodell, M. (2005). Seasonal global mean sea level change from satellite altimeter, GRACE, and geophysical models. *Journal of Geodesy*, *79*(9), 532–539.

Conkright, M. E., Locarnini, R. A., Garcia, H. E., O'Brien, T. D., Boyer, T. P., Stephens, C., et al. (2002). *World ocean atlas 2001: Objective analysis, data statistics and figures* (Internal Rep. 17, CD-ROM Doc.). Silver Spring, MD: National Oceanographic Data Center.

Dobslaw, H., Flechtner, F., Bergmann-Wolf, I., Dahle, C., Dill, R., Esselborn, S., et al. (2013). Simulating high-frequency atmosphere-ocean mass variability for de-aliasing of satellite gravity observations: AOD1B RL05. *Journal of Geophysical Research: Oceans*, *118*, 3704–3711. https://doi.org/10.1002/jgrc.20271

Dobslaw, H., & Thomas, M. (2007). Simulation and observation of global ocean mass anomalies. *Journal of Geophysical Research*, *112*, C05040. https://doi.org/10.1029/2006JC004035

Egbert, G. D., & Erofeeva, S. Y. (2002). Efficient inverse modeling of barotropic ocean tides. *Journal of Atmospheric and Oceanic Technology*, *19*, 183–204.

ESR (2009). *OSCAR third degree resolution ocean surface currents Ver. 1* (technical report). Pasadena, CA: PO.DAAC.

Everett, M. E., Constable, S., & Constable, C. G. (2003). Effects of near-surface conductance on global satellite induction responses. *Geophysical Journal International*, *153*(1), 277–286.

Forget, G., Campin, J.-M., Heimbach, P., Hill, C. N., Ponte, R. M., & Wunsch, C. (2015). ECCO version 4: An integrated framework for non-linear inverse modeling and global ocean state estimation. *Geoscientific Model Development*, *8*(10), 3071–3104.

Friis-Christensen, E., Lühr, H., & Hulot, G. (2006). *Swarm*: A constellation to study the Earth's magnetic field. *Earth Planets and Space*, *58*(4), 351–358.

Grayver, A. V., Munch, F. D., Kuvshinov, A. V., Khan, A., Sabaka, T. J., & Tøffner-Clausen, L. (2017). Joint inversion of satellite-detected tidal and magnetospheric signals constrains electrical conductivity and water content of the upper mantle and transition zone. *Geophysical Research Letters*, *44*, 6074–6081. https://doi.org/10.1002/2017GL073446

Grayver, A. V., Schnepf, N. R., Kuvshinov, A. V., Sabaka, T. J., Manoj, C., & Olsen, N. (2016). Satellite tidal magnetic signals constrain oceanic lithosphere-asthenosphere boundary. *Science Advances*, *2*(9), e1600798.

Guinehut, S., Dhomps, A. L., Larnicol, G., & Le Traon, P.-Y. (2012). High resolution 3-D temperature and salinity fields derived from in situ and satellite observations. *Ocean Science*, *8*(5), 845–857.

IOC, SCOR, and APSO (2010). The international thermodynamic equation of seawater–2010: Calculation and use of thermodynamic properties In *Intergovernmental oceanographic commission, manuals and guides* (Vol. 56, 196 p.). Paris, France: UNESCO.

Irrgang, C., Saynisch, J., & Thomas, M. (2016a). Impact of variable seawater conductivity on motional induction simulated with an ocean general circulation model. *Ocean Science*, *12*(1), 129–136.

Irrgang, C., Saynisch, J., & Thomas, M. (2016b). Ensemble simulations of the magnetic field induced by global ocean circulation: Estimating the uncertainty. *Journal of Geophysical Research: Oceans*, *121*, 1866–1880. https://doi.org/10.1002/2016JC011633

Irrgang, C., Saynisch, J., & Thomas, M. (2017). Utilizing oceanic electromagnetic induction to constrain an ocean general circulation model: A data assimilation twin experiment. *Journal of Advances in Modeling Earth Systems*, *9*, 1703–1720. https://doi.org/10.1002/2017MS000951

Ivchenko, V. O., Sidorenko, D., Danilov, S., Losch, M., & Schröter, J. (2011). Can sea surface height be used to estimate oceanic transport variability? *Geophysical Research Letters*, *38*, L11601. https://doi.org/10.1029/2011GL047387

Kuvshinov, A., Junge, A., & Utada, H. (2006). 3-D modelling the electric field due to ocean tidal flow and comparison with observations. *Geophysical Research Letters*, *33*, L06314. https://doi.org/10.1029/2005GL025043

Kuvshinov, A. V. (2008). 3-D global induction in the oceans and solid Earth: Recent progress in modeling magnetic and electric fields from sources of magnetospheric, ionospheric and oceanic origin. *Surveys in Geophysics*, *29*(2), 139–186.

Larsen, J. C. (1991). Transport measurements from in-service undersea telephone cables. *IEEE Journal of Oceanic Engineering*, *16*(4), 313–318.
Laske, G., & Masters, G. (1997). A global digital map of sediment thickness, *Eos, Transactions of the American Geophysical Union*, 78(46), Fall Meeting Supplement F483.
Le Bars, D., Durgadoo, J. V., Dijkstra, H. A., Biastoch, A., & De Ruijter, W. P. M. (2014). An observed 20-year time series of Agulhas leakage. *Ocean Science*, *10*(4), 601–609.
Leeuwenburgh, O., & Stammer, D. (2002). Uncertainties in altimetry-based velocity estimates. *Journal of Geophysical Research*, *107*(C10), 3175. https://doi.org/10.1029/2001JC000937
Locarnini, R. A., Mishonov, A. V., Antonov, J. I., Boyer, T. P., Garcia, H. E., Baranova, O. K., et al. (2013). *World ocean atlas 2013, volume 1: Temperature* (Tech. Rep. 73). Silver Spring, MD: NOAA.
Love, J. J., & Rigler, E. J. (2014). The magnetic tides of Honolulu. *Geophysical Journal International*, *197*(3), 1335–1353.
Luther, D. S., Filloux, J. H., & Chave, A. D. (1991). Low-frequency, motionally induced electromagnetic-fields in the ocean. 2. Electric-field and Eulerian current comparison. *Journal of Geophysical Research*, *96*(C7), 12797–12814. https://doi.org/10.1029/91JC00884
Manoj, C., Kuvshinov, A., Maus, S., & Lühr, H. (2006). Ocean circulation generated magnetic signals. *Earth Planets and Space*, *58*(4), 429–437.
Mellor, G. L. (1996). *Introduction to physical oceanography* (260 p.). Berlin, Germany: Springer-Verlag.
Mulet, S., Rio, M.-H., Mignot, A., Guinehut, S., & Morrow, R. (2012). A new estimate of the global 3D geostrophic ocean circulation based on satellite data and in-situ measurements. *Deep Sea Research Part II: Topical Studies in Oceanography*, *77 80–*, 70–81.
Püthe, C., Kuvshinov, A., Khan, A., & Olsen, N. (2015). A new model of Earth's radial conductivity structure derived from over 10 yr of satellite and observatory magnetic data. *Geophysical Journal International*, *203*(3), 1864–1872.
Sabaka, T. J., Olsen, N., Tyler, R. H., & Kuvshinov, A. (2015). CM5, a pre-Swarm comprehensive geomagnetic field model derived from over 12 yr of CHAMP, Orsted, SAC-C and observatory data. *Geophysical Journal International*, *200*(3), 1596–1626.
Sabaka, T. J., Tyler, R. H., & Olsen, N. (2016). Extracting ocean-generated tidal magnetic signals from swarm data through satellite gradiometry. *Geophysical Research Letters*, *43*, 3237–3245. https://doi.org/10.1002/2016GL068180
Saynisch, J., Petereit, J., Irrgang, C., Kuvshinov, A., & Thomas, M. (2016). Impact of climate variability on the tidal oceanic magnetic signal: A model based sensitivity study. *Journal of Geophysical Research: Oceans*, *121*, 5931–5941. https://doi.org/10.1002/2016JC012027
Saynisch, J., Petereit, J., Irrgang, C., & Thomas, M. (2017). Impact of oceanic warming on electromagnetic oceanic tidal signals: A CMIP5 climate model-based sensitivity study. *Geophysical Research Letters*, *44*, 4994–5000. https://doi.org/10.1002/2017GL073683
Schnepf, N. R. (2017). Going electric: Incorporating marine electromagnetism into ocean assimilation models. *Journal of Advances in Modeling Earth Systems*, *9*, 1772–1775. https://doi.org/10.1002/2017MS001130
Schnepf, N. R., Kuvshinov, A., & Sabaka, T. (2015). Can we probe the conductivity of the lithosphere and upper mantle using satellite tidal magnetic signals? *Geophysical Research Letters*, *42*, 3233–3239. https://doi.org/10.1002/2015GL063540
Schnepf, N. R., Manoj, C., Kuvshinov, A., Toh, H., & Maus, S. (2014). Tidal signals in ocean-bottom magnetic measurements of the Northwestern Pacific: Observation versus prediction. *Geophysical Journal International*, *198*(2), 1096–1110.
Tyler, R. H., Boyer, T. P., Minami, T., Zweng, M. M., & Reagan, J. R. (2017). Electrical conductivity of the global ocean. *Earth Planets and Space*, *69*(1), 156.
Tyler, R. H., Maus, S., & Lühr, H. (2003). Satellite observations of magnetic fields due to ocean tidal flow. *Science*, *299*(5604), 239–241.
Uppala, S., Dee, D., Kobayashi, S., Berrisford, P., & Simmons, A. (2008). *Toward a climate data assimilation system: Status update of ERA-interim* (Newsletter 115, pp. 12–18). Reading, UK: ECMWF.
van Sebille, E., Beal, L. M., & Biastoch, A. (2010). Sea surface slope as a proxy for Agulhas current strength. *Geophysical Research Letters*, *37*, L09610. https://doi.org/10.1029/2010GL042847
Vignudelli, S., Cipollini, P., Roblou, L., Lyard, F., Gasparini, G. P., Manzella, G., et al. (2005). Improved satellite altimetry in coastal systems: Case study of the Corsica channel (Mediterranean Sea). *Geophysical Research Letters*, *32*, L07608. https://doi.org/10.1029/2005GL022602
Vinogradova, N. T., Ponte, R. M., & Stammer, D. (2007). Relation between sea level and bottom pressure and the vertical dependence of oceanic variability. *Geophysical Research Letters*, *34*, L03608. https://doi.org/10.1029/2006GL028588
Vivier, F., Maier-Reimer, E., & Tyler, R. H. (2004). Simulations of magnetic fields generated by the Antarctic circumpolar current at satellite altitude: Can geomagnetic measurements be used to monitor the flow? *Geophysical Research Letters*, *31*, L10306. https://doi.org/10.1029/2004GL019804
Willis, J. K., Roemmich, D., & Cornuelle, B. (2004). Interannual variability in upper ocean heat content, temperature, and thermosteric expansion on global scales. *Journal of Geophysical Research*, *109*, C12036. https://doi.org/10.1029/2003JC002260
Woodworth, P. L., Vassie, J. M., Hughes, C. W., & Meredith, M. P. (1996). A test of the ability of TOPEX/POSEIDON to monitor flows through the drake passage. *Journal of Geophysical Research*, *101*(C5), 11935–11947. https://doi.org/10.1029/96JC00350
Zweng, M. M., Reagan, J. R., Antonov, J. I., Locarnini, R. A., Mishonov, A. V., Boyer, T. P., et al.. (2013). *World ocean atlas 2013, volume 2: Salinity* (Tech. Rep. 74). Silver Spring, MD: NOAA.